Ice sheet modulation of deglacial North American Monsoon intensification

Tripti Bhattacharya[1],[2], Jessica E. Tierney[1], Jason A. Addison[3], James W. Murray[4]

[1]*Department of Geosciences, University of Arizona, Tucson, AZ, USA.*

[2]*Department of Earth Sciences, Syracuse University, Syracuse, NY, USA.*

[3]*U.S. Geological Survey, Menlo Park, CA, USA.*

[4]*School of Oceanography, University of Washington, Seattle, WA, USA.*

The North American Monsoon, the dominant source of rainfall for much of the arid US Southwest, remains one of the least understood monsoon systems. The late Pleistocene evolution of this monsoon is poorly constrained, largely because glacial changes in winter rainfall obscure summer monsoon signatures in many regional proxy records. Here, we develop deglacial records of monsoon strength from isotopic analyses of leaf wax biomarkers in marine sediment cores. Reconstructions indicate a regional decrease in monsoon rainfall during the Last Glacial Maximum, and that the deglacial trajectory of the North American Monsoon closely tracks changes in North American ice cover. In climate model simulations, North American ice cover shifts the westerlies southward, favoring mixing of cold, dry air into the Southwest. This process, known as 'ventilation', weakens the monsoon by diluting the energy fluxes required for convection. As the ice sheet retreats north, the monsoon strengthens, and local ocean conditions may play a larger role in regulating its intensity. We conclude that on glacial-interglacial timescales, ice sheet-induced reorganizations of atmospheric circulation

have a dominant influence on the North American Monsoon.

Motivation

The North American Monsoon (NAM) provides over 50% of annual rainfall in arid regions of the American Southwest and northwestern Mexico, sustaining a growing human population and unique regional ecosystems[1,2]. The NAM is a summertime circulation driven by the development of a surface thermal low and upper level anti-cyclone over the desert Southwest, which draws in moist air along the Sierra Madre Occidental[3,4]. The Gulf of California (GoC) and eastern Pacific are likely the primary source of moisture in the core region [5], although the Gulf of Mexico and evapotranspiration may be important secondary sources [6–9]. Seasonal warming of Gulf of California (GoC) sea-surface temperatures (SSTs) are tightly correlated with NAM intensification, suggesting that they may help trigger convection [3,10,11]. However, remote forcing and changes in the large-scale atmospheric circulation are also important, as intraseasonal breaks in monsoon activity are linked to southward displacements of the westerlies [4,12,13].

The future trajectory of this monsoon in response to anthropogenic warming remains uncertain: climate models predict a delay in the NAM's onset by the end of the 21st century, but disagree whether increases in late-season rainfall will compensate for early season deficits[14–16]. This uncertainty highlights the need for an improved mechanistic understanding of this monsoon's response to past and present climate change. In particular, it is critical to assess the relative influence of changes to local energy fluxes and the large-scale atmospheric circulation on the long-term history and variability of the NAM.

Paleoclimate histories provide an ideal opportunity to elucidate these mechanisms. For instance, the dramatic changes in Earth's boundary conditions associated with Pleistocene glaciations may be used to analyze NAM sensitivity to a cooler global climate[17]. However, the causes of NAM changes during the Last Glacial Maximum (LGM, 21 ka BP) remain unclear. Previous paleoclimatic research hypothesized that the NAM collapsed during the LGM due to cooler oceans and continental ice sheets[18–20]. Drawing on observations of modern climate, researchers have suggested a tight link between GoC SSTs and monsoon strength over the Holocene[21,22], but it is unclear whether this SST-monsoon connection can explain NAM variability during full glacial conditions. In contrast, several modeling studies suggest that ice sheet-induced displacements of the westerlies during the LGM weakened or eliminated the NAM[20,23]. This could have resulted from 'ventilation,' or the mixing of cold, dry air into the NAM region[23]. Evaluating the relative importance of these oceanic versus atmospheric drivers of NAM strength requires high-resolution records of the monsoon during the Pleistocene-Holocene transition.

Unfortunately, large winter rainfall changes almost wholly mask the NAM signal in many deglacial proxy records[24–26], resulting in disparate descriptions of late Pleistocene NAM behavior. A composite speleothem record from southern Mexico suggests that rainfall is relatively insensitive to glacial boundary conditions[27], contradicting lacustrine records in northern Mexico that point to a weak monsoon prior to the Holocene[28,29]. The persistence of monsoon-sensitive taxa during the LGM indicates that the NAM circulation was not entirely suppressed through the last glacial interval [30], contradicting hypotheses of NAM collapse at the LGM[20]. Even among records that show dry LGM conditions, records disagree on the relative magnitude of LGM versus deglacial climate changes [31]. These divergent proxy interpretations highlight the need for quantitative paleoclimatic records that constrain the magnitude of LGM NAM changes and the monsoon's deglacial trajectory.

Leaf wax-based monsoon reconstructions

We generated new reconstructions of NAM hydroclimate using the isotopic composition of leaf wax biomarkers preserved in marine sediment cores from across the modern NAM region (Figure 1). Analysis of a north-south transect of core top samples from the Gulf of California demonstrates that leaf wax-based inferences of δD precipitation closely tracks changes in the proportion of annual rainfall that comes from the monsoon (% July-September rainfall), showing that this proxy method can provide novel constraints on NAM history (Figure 1, see Methods). We developed a Bayesian regression model to capture the strong linear relationship between leaf wax δD and % July-September rainfall (Figure 1), and then applied this regression downcore to develop continuous, quantitative estimates of NAM hydroclimate spanning the last $\sim$20,000 years.

Our reconstructions reveal dramatic changes in the monsoon's contribution to regional hydrology across the Pleistocene-Holocene transition. In the modern climatology, the Guaymas Basin receives approximately 70% of annual rainfall during the modern monsoon season. In contrast, LGM data suggest a starkly different climatology, with the summer monsoon contributing only 42% of annual rainfall (Figure 2a). Similar deglacial hydroclimate trends are evident in the core from the Mexican margin, although both records show different trajectories of monsoon change during the Holocene. This site receives 75% of annual rainfall between July and September, but more negative values of leaf wax δD at the LGM indicate that the monsoon only contributed 45-50% of annual rainfall at this time (Figure 2b, Supplementary Figure 1). Most notably, both records suggest that while the NAM was weaker at the LGM, it still comprised greater than 20% of regional rainfall. The leaf wax records also lack significant responses to known abrupt climate change events during the last deglaciation (Heinrich Stadial 1, 17.5-14.5 ka; and the Younger Dryas, 12.8-11.5 ka) (Figure 2a,b). This suggests that the deglacial NAM was not sensitive to Gulf of Mexico moisture fluxes, since the latter region cooled significantly during the Younger Dryas[32]. It also contrasts with oceanic proxies that indicate abrupt deglacial changes in upwelling intensity and temperature in the Guaymas Basin[21,33,34], and some continental records of southwest hydroclimate[25,28].

Compilations of proxy evidence from the western US show that changes in westerly-driven storms increased winter rainfall during the LGM, which could account for the large seasonality change in our reconstructions[26]. We performed a sensitivity test to identify the magnitude of winter rainfall changes needed to fully explain the LGM change in % July-September contribution (i.e. assuming that the monsoon did not change and cool season (Nov-May) precipitation was the sole driver) (Figure 3). At the Guaymas Basin, winter precipitation would have to increase between 200% and 430% to explain observed LGM proxy values; at the Mexican margin site it would have to increase 450–1420%. Such large-magnitude increases in winter rainfall are unrealistic, especially given that Clausius-Clapeyron scaling suggests that the cooler glacial atmosphere would have held less water vapor. In addition, a suite of fully-coupled GCM simulations of the LGM from the PMIP3 archive suggests that LGM winter precipitation was at most 180% greater than pre-industrial values (Figure 3b)[17]. The inferred % July-September changes from our biomarker data therefore require a substantial decrease in the strength of the summer monsoon during the LGM.

Proxy-model comparisons

To evaluate the causal mechanisms responsible for monsoon changes, we plotted our % July-September rainfall reconstructions against the temporal evolution of the Laurentide Ice Sheet[35] (Figure 2, 4). We also compared our Guaymas Basin % July-September record to SST reconstructions from the same site[34]. Deglacial SST data does not yet exist for the Mexican Margin or other regions of the GoC. % monsoon rainfall increases in step with the northward retreat of ice until the Laurentide's southern latitude crosses 55°N in both proxy records (Figure 4a). This relationship is statistically significant ($p < 0.05$, Supplementary Table 3) and can be described with a second order polynomial, with a steeper rate of increase in % monsoon rainfall at the Guaymas Basin than at the Mexican margin. The Guaymas site may be more sensitive to glacial climate changes because it sits farther north within the NAM region (Supplementary Table 3). We also analyzed the deglacial dynamics of the monsoon in a series of 'timeslice' simulations conducted with the HadCM3 climate model[36,37]. In these simulations, % July-September rainfall shows a similar polynomial relationship with the extent of the Laurentide ice sheet as observed in our proxy reconstructions (Figure 4b). The modeled relationship is driven by changes in monsoonal rainfall, and shows little correlation with winter rainfall anomalies (Supplementary Figure 2), reinforcing our interpretation that the leaf wax records ultimately reflect changes in NAM circulation.

The relationship between monsoon rain and SST at the Guaymas Basin changes sign over the deglaciation. Prior to 15 ka, monsoon strength is negatively correlated with SST (Figure 4c, Supplementary Table 3). Between 22 and 15 ka, the warmest SSTs coincide with the lowest % monsoon values. After 15 ka, monsoon rainfall covaries positively with SSTs, plateauing at modern values once SSTs are greater than 22°C. The latter relationship can be described by a quadratic polynomial (Figure 4c, Supplementary Table 3), and supports interpretations that GoC SSTs must surpass a certain threshold to sustain a strong NAM circulation[11,21]. However, the decoupling of ocean temperature and the monsoon between 22 and 15 ka suggests that some other factor must be responsible for the steady increase in monsoon strength in this interval. We suggest this may result from changes to the large-scale environment that render it unfavorable for NAM convection, independent of relatively warm SSTs. HadCM3 simulations fail to capture this 'threshold' relationship between SSTs and the NAM (Figure 4d). This may reflect the fact that many GCMs lack the resolution to explicitly simulate the GoC, which biases GCM predictions of the NAM's response to warming[14]. However, both models and proxies simulate a steady increase in monsoon strength over the deglaciation, suggesting that this bias does not play a significant role in simulations of deglacial climate. In sum, the proxy data suggest a close, consistent relationship between the NAM and ice volume during full glacial conditions, with SSTs playing a role only after 15 ka. Models support this proxy interpretation, showing a first-order influence of ice volume on changes in NAM strength across the entire deglaciation.

Influence of mid-latitude circulations on the glacial NAM

The modeled relationship between NAM intensity and ice extent results from changes in the mid-latitude westerlies. The high albedo of the Laurentide Ice Sheet creates a strong meridional gradient of temperature, which drives a southward shift in the subtropical jet based on thermal wind balance[23]. Across the timeslice simulations, the strength of westerly wind anomalies over the NAM region tracks changes in the southernmost latitude of ice over North America (Supplementary Figure 3a). Stronger westerly winds are associated with a large-scale environment that is less favorable to monsoonal convection, as indicated by the negative correlation between moist static energy and zonal wind strength over the NAM region (Supplementary Figure 3b). Decreases in moist static energy result from ventilation, or the import of low-energy air into the NAM region by the westerlies as well as the mixing influence of transient eddies[23]. These processes act synergistically, since a southward shift in the mid-latitude westerlies generates baroclinic instability, which would promote the growth of transient eddies[23].

Our work provides novel quantitative constraints on the glacial NAM circulation. The new reconstructions help resolve disagreement between evidence of a strong monsoon at the LGM[30] and studies that hypothesized the total collapse of the NAM[20] by showing that the circulation was much weaker but still present. HadCM3 simulations indicate that extensive continental ice sheets regulate the NAM by strengthening and shifting the mid-latitude westerlies, favoring the mixing of low energy air into the monsoon region. This 'ventilation effect' inhibits convection and decreases the strength of the NAM. As continental ice disintegrates, the westerlies weaken and shift northward, allowing the monsoon to intensify. This mechanism explains the strong relationship between the NAM and ice cover observed in both proxy data and model simulations. Local SSTs may have played a role in NAM strengthening towards the end of Termination 1 but they cannot explain NAM changes prior to 15 ka. The primacy of ice sheet influence distinguishes the NAM from the Indian and west African monsoons, where abrupt deglacial SST changes are dominant drivers of monsoon responses[38,39]. This strong influence of ventilation on the NAM may be tied to its geographical setting; the lack of topographic barriers against the intrusion of mid-latitude circulations, as well as the monsoon's proximity to cold, dry air over the northeast Pacific [4] may create a strong sensitivity to changes in mid-latitude atmospheric circulation [23].

Our results support the conclusions of new research that link mid-latitude circulations to the dynamics of monsoon regimes. Paleoclimate model simulations show that ventilation may regulate the poleward extent of the west African monsoon[40]. In addition, Cenozoic changes in Himalayan topography may have strengthened the south Asian monsoon by blocking ventilation by dry air from mid-latitude deserts[41,42]. Proxy-model syntheses have revealed a tight link between east Asian monsoon variability and the seasonal cycle of the westerly jet[43] as a result of enhanced energy advection downstream of Tibet[44]. Similarly, both our proxy reconstructions and model simulations support a strong role for mid-latitude circulations in modulating North American monsoon behavior on glacial-interglacial timescales. Together, this body of evidence suggests that predicting monsoon responses to past and future climate change requires careful consideration of how changes in the large-scale atmospheric flow may alter the energetic environment for convection.

Methods

Age Models. The composite record from the Guaymas Basin is based on three sediment cores: MD02-2515, JPC-56, and MD02-2517. MD02-2515 and JPC-56 have published age models based on planktic foraminifera and bulk organic carbon[33,46]. Our age model updates previous efforts by using the most recent marine calibration curve (Marine13) and a reservoir age correction based on ref.[47] (Supplementary Figure 4). The age model for MD02-2517 is based on eight radiocarbon dates on benthic and planktic foraminifera, to which we applied published benthic-planktic and reservoir age corrections[46,47] (Supplementary Table 1). The age model for NH-8P, the sediment core from the Mexican margin, is based on published radiocarbon dates on bulk organic matter[48]. For all sites, we used the Bayesian age modeling program BACON to explicitly model sedimentation rates and quantify age uncertainty (Supplementary Figure 4)[49]. Median offsets between previously published and revised age models are 100-200 years.

Leaf Wax Analyses. Lipids were extracted from freeze-dried and homogenized sediments using an accelerated solvent extractor system (ASE, Dionex 350), at a temperature and pressure of 100°C and 1500 psi, respectively. The total lipid extract (TLE) was evaporated under a steady stream of N_2 gas. We separated fatty acids from other lipid compounds using an aminopropylsilyl gel column, eluting the neutral fraction with a dichloromethane:isopropanol (2:1) and the acid fraction with 4% acetic acid in dichloromethane. We methylated the acids in a solution of acidified methanol (50°C, overnight). The resultant FAMEs (fatty acid methyl esters) were purified again over silica gel using dichloromethane. We focused subsequent analyses on the C_{30} fatty acid, since it is exclusively derived from terrestrial plants[50].

FAME concentrations were determined using a GC-FID system. Hydrogen and carbon isotopic composition were measured via gas chromatography-isotope ratio-mass spectrometry (GC-IR-MS) using a Thermo Delta V Plus mass spectrometer. Reference H_2 and CO_2 gases were calibrated to an *n*-alkane standard (A6 mix provided by Arndt Schimmelmann at Indiana University), and a synthetic mix of FAMEs was analyzed every 5-7 samples to monitor drift. Samples were run in quadruplicate for δD to obtain a precision better than 2‰, and triplicate for δ^{13}C to obtain a precision better than 0.2‰. To account for the added methyl group during methylation, the δD and δ^{13}C of the methylation methanol was determined by methylating a phthalic acid standard of known isotopic composition obtained from Arndt Schimmelmann at Indiana University. A mass balance correction was then applied to the δD and δ^{13}C values of our FAMEs. Down-core measurements of δD were corrected for ice volume changes during glacial intervals. Benthic oxygen isotope data was used as a proxy for ice volume[51], and was then scaled assuming that 1‰ of the increase in δ^{18}O (8‰ in δD) at the LGM is due to ice alone[52]. The correction is therefore:

$$\delta D_{corrected} = \frac{1000 + \delta D_{initial}}{((8 * \delta^{18} O_{scaled})/1000) + 1} - 1000 \quad (1)$$

NAM Reconstructions. We used modern coretop data from the Gulf of California to develop a quantitative relationship between rainfall seasonality and leaf wax δD. Sediment trap studies suggest that waxes in near-shore marine settings primarily reflect local vegetation[53]. We first converted δD_{wax} values to estimates of δD_{precip}. While leaf wax hydrogen isotopes closely track the isotopic composition of environmental water and therefore $\delta\mathrm{D}_{precip}$, this relationship can be confounded by variability in the apparent offset between $\delta\mathrm{D}_{wax}$ and $\delta\mathrm{D}_{precip}$, or $\varepsilon_{water-wax}$, across different plant taxa. In particular, waxes synthesized by graminoids are more depleted relative to $\delta\mathrm{D}_{precip}$ than those produced by eudicots[50], perhaps as a result of variations in the timing of seasonal leaf wax production or in the intermediate hydrocarbon compounds used in leaf wax synthesis[54]. Limited measurements of ε values are available for members of Cactaceae, which use the Crassulaic Acid Metabolism (CAM), but this family may not be a major contributor to sedimentary leaf waxes. Carbon isotopes track changing proportions of graminoids vs. eudicots on the landscape, since herbs and shrubs in the NAM region primarily use the C_3 photosynthetic pathway, while most grasses are C_4 taxa[50]. In turn, C_3 and C_4 photosynthetic pathways result in different values of leaf wax δ^{13}C, with a more enriched carbon isotopic signature in C_4 taxa.

We used paired carbon isotopes to identify the proportion of leaf waxes that come from C_4 grasses vs. eudicots, and then applied appropriate $\varepsilon_{water-wax}$ offsets to infer $\delta\mathrm{D}_{precip}$ from $\delta\mathrm{D}_{wax}$. In this approach, we represent ε values as proportional to the fraction of C_4 (f_{C4}) taxa in a given sample of sedimentary leaf waxes (Eq. 2). This ε value is then used to adjust $\delta\mathrm{D}_{wax}$ values to obtain $\delta\mathrm{D}_{precip}$ (Eq. 3)[55].

$$\varepsilon = f_{C4} \cdot \varepsilon_{C4} + (1 - f_{C4}) \cdot \varepsilon_{C3} \tag{2}$$

$$\delta D_{precip} = \frac{1000 + \delta D_{wax}}{(\varepsilon/1000) + 1} - 1000 \tag{3}$$

Equation 2 requires us to identify a probability distribution of values of f_{C4} given a certain number of C_4 leaf waxes in each leaf-wax sample (Y), or $P(f_{C4}|Y)$. Y can be inferred from δ^{13}C data, using equation 4, where N is the number of leaf waxes in a sample (assumed to be a large number).

$$Y = (\frac{\delta^{13}C_{wax} - \delta^{13}C_{C3}}{\delta^{13}C_{C4} - \delta^{13}C_{C3}}) \cdot N \tag{4}$$

Inference proceeds in a Bayesian framework following ref. [55]. End-member δ^{13}C values were obtained from our own measurements of Sonoran desert taxa at the Arizona-Sonora Desert Museum (ASDM), near Tucson, AZ (Supplementary Table 2). Leaf samples from Sonoran desert species were gathered by student participants in the ASDM's Junior Docents program on May 17 and June 25, 2016. During each sampling effort, several leaves from separate specimens were collected and homogenized to average across individual variability. Upon transport to the lab, samples were freeze-dried and cut into 0.4 g samples. *n*-acids were extracted and measured following the same methods applied to the sedimentary leaf waxes. In total, 3 C_4 taxa and 17 C_3 taxa are included in our analysis. A full list of taxa sampled, as well as C_{30} n-acid concentrations and isotopic values, is provided in Supplementary Table 3. These values of δ^{13}C inferred from modern plants were corrected for isotopic changes in atmospheric carbon associated with the Suess effect. Corrected and uncorrected values are in Extended Tables 2 and 3.

Estimates of $\varepsilon_{water-wax}$ for C_4 and C_3 taxa are obtained from the data compilation in ref. [50]. ε values are based on the C_{29} n-alkane rather than the C_{30} n-acid; given that existing research disagrees about whether there are significant offsets between n-acid and n-alkane apparent fractionations we assume that these are equivalent[50,54]. The corrections were performed using a Bayesian framework, as detailed in ref. [55]. This carbon correction had a minimal impact on the overall trends in our data since down-core δ^{13}C changes are not large; indeed, raw δD_{wax} is strongly correlated with inferred δD_{precip} ($r = 0.92$). Down-core δD_{precip} values are shown in Supplementary Figure 1.

We analyzed the correlation between coretop δD_{precip} values and climate data from adjacent land areas using the high-resolution (0.3°) North American Regional Reanalysis (NARR)[56]. Because of known biases in NARR evaporation and moisture transports [57], we only use the precipitation and temperature, which are directly assimilated. Seasonally-averaged NARR precipitation exhibits little bias over northwest Mexico [58]. For each coretop site, terrestrial grid cells within 1° of latitude and 2° of longitude were used to determine the average climate of the region contributing leaf waxes to the coretop site. The strongest relationship is with % July-September (% JAS, $r = 0.79$) rainfall (Figure 1). This relationship reflects differences in the isotopic composition of winter and summer rainfall: the Global Network of Isotopes in Precipitation (GNIP) station in Tucson, AZ shows that summer rainfall is more enriched in deuterium relative to winter rainfall (Supplementary Figure 5), likely as a result of differences of temperature, strength of convective updrafts, and water vapor source region for each season[59,60]. Thus, sites with increased monsoon rainfall exhibit more positive rainfall δD values. This interpretation is distinct from the 'amount effect,' which would predict a more depleted isotopic signature as rainfall rates increase moving south along the Mexican Margin [61]. We suggest that seasonality dominates our isotopic signature because this region features a bimodal rainfall distribution with distinct isotopic compositions for winter and summer precipitation that swamp any signal from the amount effect. Rainfall data from Tucson reveals that the isotopic offset between winter and summer rainfall is larger than the magnitude of isotopic variability associated with interannual changes in rainfall amount [59].

Inferred δD_{precip} might reflect evaporative enrichment of leaf water, as ε in individual taxa has been shown to vary across aridity gradients [62,63]. However, this effect may be attenuated in sedimentary leaf waxes, which are bulk mixtures of multiple plant taxa that each have different environmental sensitivities to leaf water enrichment. In addition, plants in regions with a greater proportion of %July-September rainfall may register greater leaf water enrichments due to higher temperatures during wax synthesis. Thus, even if our δD signal does not record precipitation isotopes with perfect fidelity, evaporative enrichment may amplify the statistical link between wax isotopic composition and %July-September rainfall. Changes in annual temperature may influence δD values at the LGM, but any such influence is minor, as SST reconstructions from the Guaymas Basin suggest a 4°C cooling at the LGM relative to early Holocene values[34], implying a 4‰ decrease in δD.

A quantitative relationship between %JAS rainfall and δD_{precip}, as well as reconstructions of % monsoon rainfall over the deglaciation, were built using Bayesian inference following the methods outlined in ref. [55]. We developed a Bayesian regression relating δD_{precip} (Y) to % July-September rainfall (first column of X; second column of X consists of ones), where:

$$Y = X \cdot \beta + \epsilon \tag{5}$$

$$\epsilon \sim N(0, \tau^2), IID \tag{6}$$

β is a vector of regression coefficients and ϵ is the model error, with independent and identically normally-distributed errors (IID) and a variance of τ^2 (Eq. 6). We estimate the parameters using Bayes' Rule, using Normal prior distributions for β and an Inverse Gamma prior for τ^2 [55]. The conditional posterior distributions for each parameter are conjugate with the prior distributions, meaning that they follow the same distributional form[64]. Calculation of the full posterior solution for each parameter proceeds via a Gibbs sampler[64], where initial values for τ^2 and β are specified, and values are sequentially sampled from their respective conditional posterior distributions. Supplementary Figure 6 shows the prior and posterior distributions for the regression model parameters.

Our ultimate goal is to infer % JAS values from down-core measurements of $\delta\mathrm{D}_{precip}$. To do so, we must invert the regression model developed above using another application of Bayes' rule relating % JAS (X) to $\delta\mathrm{D}_{precip}$ (Y):

$$P(X|Y) \propto P(Y|X) \cdot P(X) \tag{7}$$

$P(Y|X)$ is our regression model, and $P(X)$ is a specified prior distribution. The prior distribution is Normal ($N(\mu_p, \sigma_p^2)$). The prior mean is set to modern climatological % JAS at each core site, while σ_p is set to 12, to match the observed variability in % July-September rainfall in the NARR dataset, which we take as a plausible range of values. Inference of % July-September rainfall proceeds by drawing from the suite of inferred δD_{precip} values and the posterior distribution of parameters from the regression model. This process iterates through all previously inferred down-core δD_{precip} values, so the variance at each point in our final data includes the full range of error from both our δD_{precip} reconstructions and the reconstructions of % July-September rainfall. Comparison of the prior and posterior distributions of modern inferred % July-September rainfall at each core site shows that the posterior distribution is much narrower as a result of the incorporation of the information from the δD_{precip} data (Supplementary Figure 7). In Figure 2, error envelopes represent the 68% and 95% confidence intervals for each datapoint, and also incorporate age uncertainty. For full details of the Bayesian approach, see ref [55].

HadCM3 Model Simulations. We explored the drivers of deglacial NAM changes using a series of 'timeslice' simulations conducted with the model HadCM3. HadCM3 is an Earth system model developed by the UK Meteorological Office, and consists of an atmospheric model (HadAM3) coupled to an ocean and sea ice model, as well as a land surface model[65]. The atmosphere, ocean, and sea ice components are run at a relatively coarse resolution of $2.5°$ latitude by $3.75°$ longitude [37]. Despite the coarse resolution, the pre-industrial control produces a NAM with rainfall rates comparable to instrumental data (Supplementary Figure 8). The land surface model, the Met Office Surface Exchange Scheme (MOSES2.1), includes a vegetation and terrestrial carbon model (TRIFFID) [66]. However, atmospheric concentrations of greenhouse gases (CO_2, CH_4, and N_2O)

were prescribed based on gas concentrations obtained from ice core data[36]. Orbital parameters and ice sheets were also prescribed, with the latter derived from the ICE 5G dataset[67]. Freshwater forcing in the North Atlantic associated with abrupt deglacial climate events is not included in these simulations.

'Timeslice' model simulations including dynamic vegetation for each 1,000-year timestep were initiated from a previous set of simulations and allowed to run to equilibrium[36]. The timesteps between 21 ka and 0 ka were used for the analyses in this paper. We analyzed NAM domain averages ($18 - 33$°N and $102 - 112$°W) of precipitation, sea surface temperature, air temperature, geopotential height, zonal and meridional winds, and specific humidity. We also calculated moist static energy (MSE), which measures an air column's energetic content, integrating information from the geopotential height (parcel's height z multiplied by the gravitational constant g), temperature (T multiplied by the specific heat C_p), and moisture content (specific humidity q multiplied by the latent heat of vaporization L_v) (Equation 8). MSE is conserved in adiabatic processes and broadly measures the favorability of atmospheric conditions for convection[68]. This approach is supported by the fact that the correlation between summer precipitation anomalies and changes in MSE over the NAM region is 0.86 across timeslice simulations.

$$MSE = C_p \cdot T + L_v \cdot q + g \cdot z \tag{8}$$

In these simulations, we find that % July-September rainfall, the parameter we reconstruct from leaf wax data, strongly covaries with changes in total summertime rainfall (r^2 = 0.81), and is only weakly related to winter rainfall amount (r^2=0.04) (Supplementary Figure 2). This supports our inference that % July-September rainfall changes in the NAM domain are ultimately reflecting summertime circulation.

Recent studies have suggested local land surface evapotranspiration and albedo may influence the strength of the NAM circulation [3,6,7]. The inclusion of dynamic vegetation in this model allows us to analyze the impact of changes in land surface characteristics on the NAM. In HadCM3, land surface evapotranspiration has little correlation with deglacial changes in % monsoon rainfall, and the surface albedo remains constant across simulations (Supplementary Figure 2). This suggests land surface processes have little impact on monsoon strength, but further testing of these hypotheses would benefit from regional climate model simulations.

Comparisons between reconstructed NAM changes, ice sheet extent, and SST. Our comparison between reconstructed % July-September rainfall and ice sheet extent (Figure 4a) accounts for age model and reconstructed uncertainty in a Monte Carlo fashion. We both 1) resample from the suite of age models for each sediment core to identify the full range of possible values of leaf wax δD for a given absolute calendar age interval during the deglaciation; and 2) resample the full range of error in our reconstructions of % July-September rainfall for each core site. This approach yields the complete range of possible values of % July-September rainfall for any absolute calendar age interval.

Reconstructions of ice sheet variables from the LGM to the present were obtained from the ICE6G dataset, which uses geodetic measurements of crustal motion and a dynamical model to constrain the chronology of ice sheet retreat[35,69]. The resultant model of ice sheet change is tuned using exposure dating and detailed sea-level records. We obtained values for the southernmost latitude of ice over North America for 500-year intervals from 21,000 years BP to 1,000 years BP. Since the output comes from a dynamic model, we do not account for age uncertainty. The southernmost latitude of ice correlates strongly with other metrics of ice extent, including ice area ($r = 0.93$).

After obtaining distributions of possible % July-September rainfall values for each 100-year interval during the deglaciation, we binned the results based on their corresponding value of southernmost latitude of ice from the ICE6G dataset, and constructed the 95% confidence intervals shown in Figure 4a. To illustrate the shape of the relationship, we fit these values with a second-order polynomial. Error estimates on polynomial coefficients are based on fitting a suite of polynomials to the full suite of output from our Monte Carlo simulations (Supplementary Table 4). We also calculated coefficients for HadCM3 timeslice simulations, but were not able to calculate coefficients errors since only one set of model runs were available. We assessed statistical significance by calculating the adjusted R^2 and performing a separate F-test.

Deglacial records of Gulf of California SST only exist for the Guaymas Basin, so we restrict ourselves to analyzing the relationship between SST and monsoon rainfall at the Guaymas Basin site. Future research, including the development of quantitative deglacial SST reconstructions from the Mexican Margin, will permit more rigorous testing of the relationship between regional ocean temperature and monsoon convection. The reconstruction for the Guaymas Basin is based on alkenones obtained from MD02-2515, the same core from which we extracted leaf waxes[34]. We restrict our analyses to the leaf wax reconstructions from MD02-2515, since we can control for age uncertainty when comparing measurements from the same core. In this case, we construct a scatterplot of SST vs. % July-September rainfall, and error bars in this case represent the propagation of analytical error in both leaf wax data and the alkenone data and uncertainty from our Bayesian reconstruction of % July-September rainfall.

Data Availability Statement New leaf wax-based reconstructions will be made available for download from NOAA's National Center for Environmental Information Paleoclimatology Database https://www.ncdc.noaa.gov/data-access/paleoclimatology-data, and by contacting the corresponding author. Previously published alkenone data from the Guaymas Basin are also available via the NOAA database. HadCM3 model code is available at `http://cms.ncas.ac.uk/code_browsers/UM4.5/UMbrowser/index.html`. Simulations used in this paper [37] are available at `https://www.paleo.bristol.ac.uk/ummodel/scripts/papers/Davies-Barnard_et_al_2017.html`. ICE6G data are available at `http://www.atmosp.physics.utoronto.ca/~peltier/data.php`.

1. Ray, A. J. *et al.* Applications of monsoon research: Opportunities to inform decision making and reduce regional vulnerability. *Journal of Climate* **20**, 1608–1627 (2007).

2. Turner, R., Bowers, J. & Burgess, T. *Sonoran Desert Plants: An Ecological Atlas* (University of Arizona Press, Tucson, AZ, 1995).

3. Vera, C. *et al.* Toward a unified view of the American monsoon systems. *Journal of climate* **19**, 4977–5000 (2006).

4. Adams, D. K. & Comrie, A. C. The North American Monsoon. *Bulletin of the American Meteorological Society* **78**, 2197–2213 (1997).

5. Jana, S., Rajagopalan, B., Alexander, M. A. & Ray, A. J. Understanding the dominant sources and tracks of moisture for summer rainfall in the southwest United States. *Journal of Geophysical Research: Atmospheres* **19**, 4850–4870 (2018).

6. Hu, H. & Dominguez, F. Evaluation of oceanic and terrestrial sources of moisture for the North American monsoon using numerical models and precipitation stable isotopes. *Journal of Hydrometeorology* **16**, 19–35 (2015).

7. Vivoni, E. R., Tai, K. & Gochis, D. J. Effects of initial soil moisture on rainfall generation and subsequent hydrologic response during the North American Monsoon. *Journal of Hydrometeorology* **10**, 644–664 (2009).

8. Small, E. E. The influence of soil moisture anomalies on variability of the North American Monsoon system. *Geophysical research letters* **28**, 139–142 (2001).

9. Findell, K. L., Gentine, P., Lintner, B. R. & Kerr, C. Probability of afternoon precipitation in eastern United States and Mexico enhanced by high evaporation. *Nature Geoscience* **4**, 434 (2011).

10. Erfani, E. & Mitchell, D. A partial mechanistic understanding of the North American Monsoon. *Journal of Geophysical Research: Atmospheres* **119** (2014).

11. Mitchell, D. L., Ivanova, D., Rabin, R., Brown, T. J. & Redmond, K. Gulf of California sea surface temperatures and the North American Monsoon: mechanistic implications from observations. *Journal of Climate* **15**, 2261–2281 (2002).

12. Carleton, A. M. Synoptic-dynamic character of 'bursts' and 'breaks' in the South-West US summer precipitation singularity. *International Journal of Climatology* **6**, 605–623 (1986).

13. Pascale, S. & Bordoni, S. Tropical and extratropical controls of Gulf of California surges and summertime precipitation over the southwestern United States. *Monthly Weather Review* **144**, 2695–2718 (2016).

14. Pascale, S. *et al.* Weakening of the North American Monsoon with global warming. *Nature Climate Change* (2017).

15. Meyer, J. D. & Jin, J. The response of future projections of the North American monsoon when combining dynamical downscaling and bias correction of CCSM4 output. *Climate Dynamics* **49**, 433–447 (2017).

16. Cook, B. & Seager, R. The response of the North American Monsoon to increased greenhouse gas forcing. *Journal of Geophysical Research: Atmospheres* **118**, 1690–1699 (2013).

17. Braconnot, P. *et al.* Evaluation of climate models using palaeoclimatic data. *Nature Climate Change* **2**, 417 (2012).

18. Metcalfe, S. E., O'Hara, S. L., Caballero, M. & Davies, S. J. Records of Late Pleistocene–Holocene climatic change in Mexico: a review. *Quaternary Science Reviews* **19**, 699–721 (2000).

19. Kutzbach, J. *et al.* Climate and biome simulations for the past 21,000 years. *Quaternary Science Reviews* **17**, 473–506 (1998).

20. Thompson, R. S. & Anderson, K. H. Biomes of western North America at 18,000, 6000 and 0 ^{14}C yr BP reconstructed from pollen and packrat midden data. *Journal of Biogeography* **27**, 555–584 (2000).

21. Barron, J. A., Metcalfe, S. E. & Addison, J. A. Response of the North American monsoon to regional changes in ocean surface temperature. *Paleoceanography* **27** (2012).

22. Metcalfe, S. E., Barron, J. A. & Davies, S. J. The Holocene history of the North American Monsoon:'known knowns' and 'known unknowns' in understanding its spatial and temporal complexity. *Quaternary Science Reviews* **120**, 1–27 (2015).

23. Bhattacharya, T., Tierney, J. E. & DiNezio, P. Glacial reduction of the North American Monsoon via surface cooling and atmospheric ventilation. *Geophysical Research Letters* **44**, 5113–5122 (2017).

24. Asmerom, Y., Polyak, V. J. & Burns, S. J. Variable winter moisture in the southwestern United States linked to rapid glacial climate shifts. *Nature Geoscience* **3**, 114–117 (2010).

25. Wagner, J. D. *et al.* Moisture variability in the southwestern United States linked to abrupt glacial climate change. *Nature Geoscience* **3**, 110 (2010).

26. Oster, J. L., Ibarra, D. E., Winnick, M. J. & Maher, K. Steering of westerly storms over western North America at the Last Glacial Maximum. *Nature Geoscience* **8**, 201 (2015).

27. Lachniet, M. S., Asmerom, Y., Bernal, J. P., Polyak, V. J. & Vazquez-Selem, L. Orbital pacing and ocean circulation-induced collapses of the Mesoamerican monsoon over the past 22,000 y. *Proceedings of the National Academy of Sciences* **110**, 9255–9260 (2013).

28. Roy, P. D. *et al.* Paleohydrology of the Santiaguillo Basin (Mexico) since late last glacial and climate variation in southern part of western subtropical North America. *Quaternary Research* **84**, 335–347 (2015).

29. Lozano-Garcıa, M. S., Ortega-Guerrero, B. & Sosa-Nájera, S. Mid-to late-Wisconsin pollen record of San Felipe basin, Baja California. *Quaternary Research* **58**, 84–92 (2002).

30. Holmgren, C. A., Norris, J. & Betancourt, J. L. Inferences about winter temperatures and summer rains from the late Quaternary record of C4 perennial grasses and C3 desert shrubs in the northern Chihuahuan Desert. *Journal of Quaternary Science* **22**, 141–161 (2007).

31. Roy, P. D. *et al.* Late Quaternary paleohydrological conditions in the drylands of northern Mexico: a summer precipitation proxy record of the last 80 cal ka BP. *Quaternary Science Reviews* **78**, 342–354 (2013).

32. Schmidt, M. W. & Lynch-Stieglitz, J. Florida Straits deglacial temperature and salinity change: Implications for tropical hydrologic cycle variability during the Younger Dryas. *Paleoceanography* **26** (2011).

33. Pichevin, L. *et al.* Silicic acid biogeochemistry in the Gulf of California: Insights from sedimentary Si isotopes. *Paleoceanography* **27** (2012).

34. McClymont, E. L. *et al.* Sea-surface temperature records of Termination 1 in the Gulf of California: Challenges for seasonal and interannual analogues of tropical Pacific climate change. *Paleoceanography* **27** (2012).

35. Peltier, W., Argus, D. & Drummond, R. Space geodesy constrains ice age terminal deglaciation: The global ICE-6G_C (VM5a) model. *Journal of Geophysical Research: Solid Earth* **120**, 450–487 (2015).

36. Singarayer, J. S. & Valdes, P. J. High-latitude climate sensitivity to ice-sheet forcing over the last 120kyr. *Quaternary Science Reviews* **29**, 43–55 (2010).

37. Davies-Barnard, T., Ridgwell, A., Singarayer, J. & Valdes, P. Quantifying the influence of the terrestrial biosphere on glacial-interglacial climate dynamics. *Climate of the Past* **13**, 1381–1401 (2017).

38. Tierney, J. E., Pausata, F. S. *et al.* Deglacial Indian monsoon failure and North Atlantic stadials linked by Indian Ocean surface cooling. *Nature Geoscience* **9**, 46–50 (2016).

39. Chang, P. *et al.* Oceanic link between abrupt changes in the North Atlantic Ocean and the African monsoon. *Nature Geoscience* **1**, 444 – 448 (2008).

40. Su, H. & Neelin, J. D. Dynamical mechanisms for African monsoon changes during the mid-Holocene. *Journal of Geophysical Research: Atmospheres* **110** (2005).

41. Molnar, P., Boos, W. R. & Battisti, D. S. Orographic controls on climate and paleoclimate of Asia: thermal and mechanical roles for the Tibetan Plateau. *Annual Review of Earth and Planetary Sciences* **38** (2010).

42. Boos, W. R. A review of recent progress on Tibet's role in the South Asian monsoon. *CLIVAR Exch* **19**, 23–27 (2015).

43. Chiang, J. C. *et al.* Role of seasonal transitions and westerly jets in East Asian paleoclimate. *Quaternary Science Reviews* **108**, 111–129 (2015).

44. Chen, J. & Bordoni, S. Orographic effects of the Tibetan Plateau on the East Asian summer monsoon: An energetic perspective. *Journal of Climate* **27**, 3052–3072 (2014).

45. Schneider, U. *et al.* Gpcc's new land surface precipitation climatology based on quality-controlled in situ data and its role in quantifying the global water cycle. *Theoretical and Applied Climatology* **115**, 15–40 (2014).

46. Keigwin, L. D. Late Pleistocene-Holocene paleoceanography and ventilation of the Gulf of California. *Journal of Oceanography* **58**, 421–432 (2002).

47. Goodfriend, G. A. & Flessa, K. W. Radiocarbon reservoir ages in the Gulf of California: roles of upwelling and flow from the Colorado River. *Radiocarbon* **39**, 139–148 (1997).

48. Ganeshram, R. S. & Pedersen, T. F. Glacial-interglacial variability in upwelling and bioproductivity off NW Mexico: implications for Quaternary paleoclimate. *Paleoceanography* **13**, 634–645 (1998).

49. Blaauw, M., Christen, J. A. *et al.* Flexible paleoclimate age-depth models using an autoregressive gamma process. *Bayesian analysis* **6**, 457–474 (2011).

50. Sachse, D. *et al.* Molecular paleohydrology: interpreting the hydrogen-isotopic composition of lipid biomarkers from photosynthesizing organisms. *Annual Review of Earth and Planetary Sciences* **40**, 221–249 (2012).

51. Lisiecki, L. E. & Raymo, M. E. A Pliocene-Pleistocene stack of 57 globally distributed benthic δ18O records. *Paleoceanography* **20** (2005).

52. Schrag, D. P., Hampt, G. & Murray, D. W. Pore fluid constraints on the temperature and oxygen isotopic composition of the glacial ocean. *Science* **272**, 1930–1932 (1996).

53. Schreuder, L. T., Stuut, J.-B. W., Korte, L. F., Damsté, J. S. S. & Schouten, S. Aeolian transport and deposition of plant wax n-alkanes across the tropical North Atlantic Ocean. *Organic Geochemistry* **115**, 113–123 (2018).

54. Gao, L., Edwards, E. J., Zeng, Y. & Huang, Y. Major evolutionary trends in hydrogen isotope fractionation of vascular plant leaf waxes. *PloS one* **9**, e112610 (2014).

55. Tierney, J. E., Pausata, F. S. *et al.* Rainfall regimes of the Green Sahara. *Science advances* **3**, e1601503 (2017).

56. Mesinger, F. *et al.* North American Regional Reanalysis. *Bulletin of the American Meteorological Society* **87**, 343–360 (2006).

57. Nigam, S. & Ruiz-Barradas, A. Seasonal hydroclimate variability over North America in global and regional reanalyses and AMIP simulations: Varied representation. *Journal of Climate* **19**, 815–837 (2006).

58. Mo, K. C., Chelliah, M., Carrera, M. L., Higgins, R. W. & Ebisuzaki, W. Atmospheric moisture transport over the United States and Mexico as evaluated in the NCEP Regional Reanalysis. *Journal of Hydrometeorology* **6**, 710–728 (2005).

59. Eastoe, C. & Dettman, D. Isotope amount effects in hydrologic and climate reconstructions of monsoon climates: Implications of some long-term data sets for precipitation. *Chemical Geology* **430**, 78–89 (2016).

60. Aggarwal, P. K. *et al.* Stable isotopes in global precipitation: A unified interpretation based on atmospheric moisture residence time. *Geophysical Research Letters* **39** (2012).

61. Risi, C., Bony, S. & Vimeux, F. Influence of convective processes on the isotopic composition (δ18o and δd) of precipitation and water vapor in the tropics: 2. physical interpretation of the amount effect. *Journal of Geophysical Research: Atmospheres* **113** (2008).

62. Kahmen, A. *et al.* Leaf water deuterium enrichment shapes leaf wax n-alkane δd values of angiosperm plants ii: Observational evidence and global implications. *Geochimica et Cosmochimica Acta* **111**, 50–63 (2013).

63. Berke, M. A., Tipple, B. J., Hambach, B. & Ehleringer, J. R. Life form-specific gradients in compound-specific hydrogen isotope ratios of modern leaf waxes along a North American Monsoonal transect. *Oecologia* **179**, 981–997 (2015).

64. Gelman, A. *et al.* *Bayesian data analysis*, vol. 2 (CRC press Boca Raton, FL, 2014).

65. Valdes, P. J. *et al.* The BRIDGE HadCM3 family of climate models: HadCM3@ Bristol v1. 0. *Geoscientific Model Development Discussions* (2017).

66. Cox, P. M. Description of the TRIFFID dynamic global vegetation model. *Hadley Centre Technical Note* **24**, 1–16 (2001).

67. Peltier, W. Global glacial isostasy and the surface of the ice-age Earth: the ICE-5G (VM2) model and GRACE. *Annu. Rev. Earth Planet. Sci.* **32**, 111–149 (2004).

68. Holton, J. R. & Hakim, G. J. *An introduction to dynamic meteorology*, vol. 88 (Academic press, 2012).

69. Argus, D. F., Peltier, W., Drummond, R. & Moore, A. W. The Antarctica component of postglacial rebound model ICE-6G_C (VM5a) based on GPS positioning, exposure age dating of ice thicknesses, and relative sea level histories. *Geophysical Journal International* **198**, 537–563 (2014).

Acknowledgements Support for this research comes from the David and Lucile Packard Foundation Fellowship in Science and Engineering to J.E.T. and NSF grant OCE-1651034 to J.E.T. We thank Amy Orchard and the Junior Docents at the Arizona-Sonora Desert Museum for assistance with leaf collection, and Jeshua Case-Gonzalez, Nicholas Montiel, Patrick Murphy, and Paul Zander for assistance with preparation and analysis of the Sonoran desert plant samples. Access to core samples and coretops was facilitated by the British Ocean Sediment Core Research Facility (BOSCORF), the Geological and Oceanographic Collections at Scripps Institute of Oceanography, and the Marine and Geology Repository at Oregon State University (OSU) (NSF OCE-1558679). We thank Paul Valdes at Bristol for providing access to the HadCM3 timeslice simulations. We thank John Barron and Summer Praetorius (USGS) for their guidance with age models and insights on the Gulf of California. J.A.A. is supported by the USGS Climate Research and

Development Program. Upon publication, the proxy records contained in this data will be archived in the NOAA Paleoclimatology Database. We thank three anonymous reviewers and one internal USGS reviewer for insightful comments that greatly improved this manuscript.

Author Contributions T.B. and J.E.T. designed the study, collected the data, and performed the data analysis. J.A.A. and J.W.M. provided access to samples and assisted in data collection. T.B. and J.E.T. wrote the manuscript.

Competing Interests The authors declare that they have no competing financial interests.

Correspondence Correspondence and requests for materials should be addressed to T.B. (email: tripti@email.arizona.edu).

1 Main Text Figure Captions

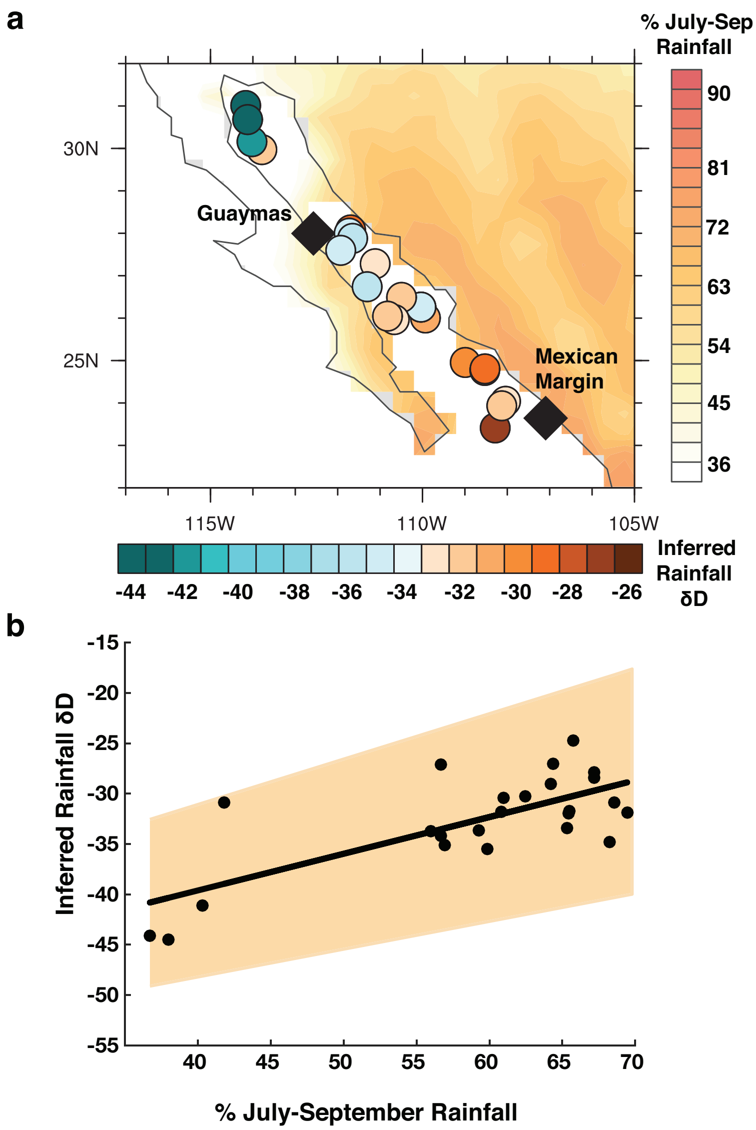

Figure 1: Relationship between leaf waxes δD and monsoon rainfall. a) core sites (diamonds) and coretop data (circles) with leaf wax-inferred δD of precipitation (colors of circles). Color contours show climatological % July-September (monsoon season) rainfall [45]. b) Bayesian regression between coretop leaf-wax inferred δD_{precip} and %July-September rainfall, with the 95% confidence interval.

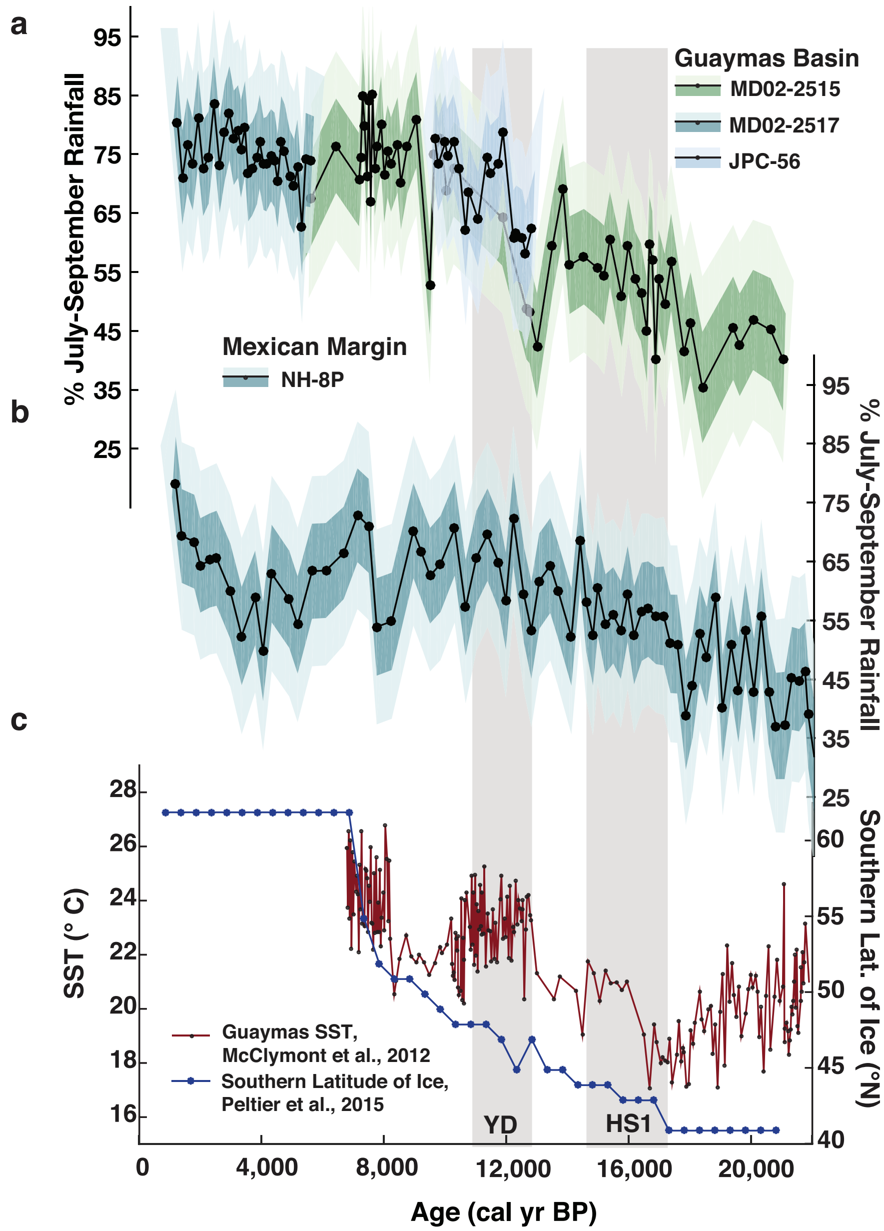

Figure 2: Leaf-wax based reconstructions of % July-September rainfall at the Guaymas Basin (a) and Mexican Margin (b) sites. Dark and light error bars indicate 1σ and 2σ uncertainties in the reconstructions respectively, while the central black line indicates the mean value. c) shows changes in regional forcings, including the southernmost latitudinal extent of the Laurentide ice sheet[35] and Guaymas Basin SSTs [34]. Gray bars highlight the Younger Dryas (YD; 12.8-11.5 ka) and Heinrich Stadial 1 (HS1; 17.5-14.5 ka).

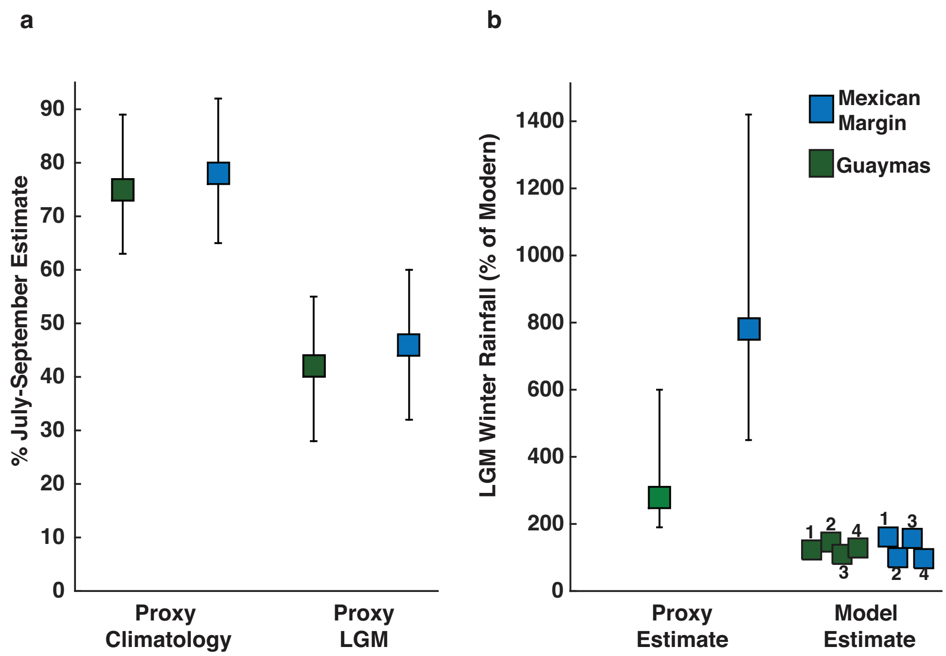

Figure 3: Sensitivity of monsoon reconstructions to winter rainfall changes. a) Modern proxy-estimated values of % July-September rainfall for each core site versus proxy estimates of LGM values (averaged between 22 and 18 ka). b) shows % change in November-March rainfall needed if winter rainfall was the sole driver of deglacial % JAS changes. Error bars represent 95% confidence intervals. Model estimates of changes in winter rainfall are included from PMIP3 archive [17], with 1=CNRM-CM4, 2=CCSM4, 3=MPI-ESM, and 4=MIROC.

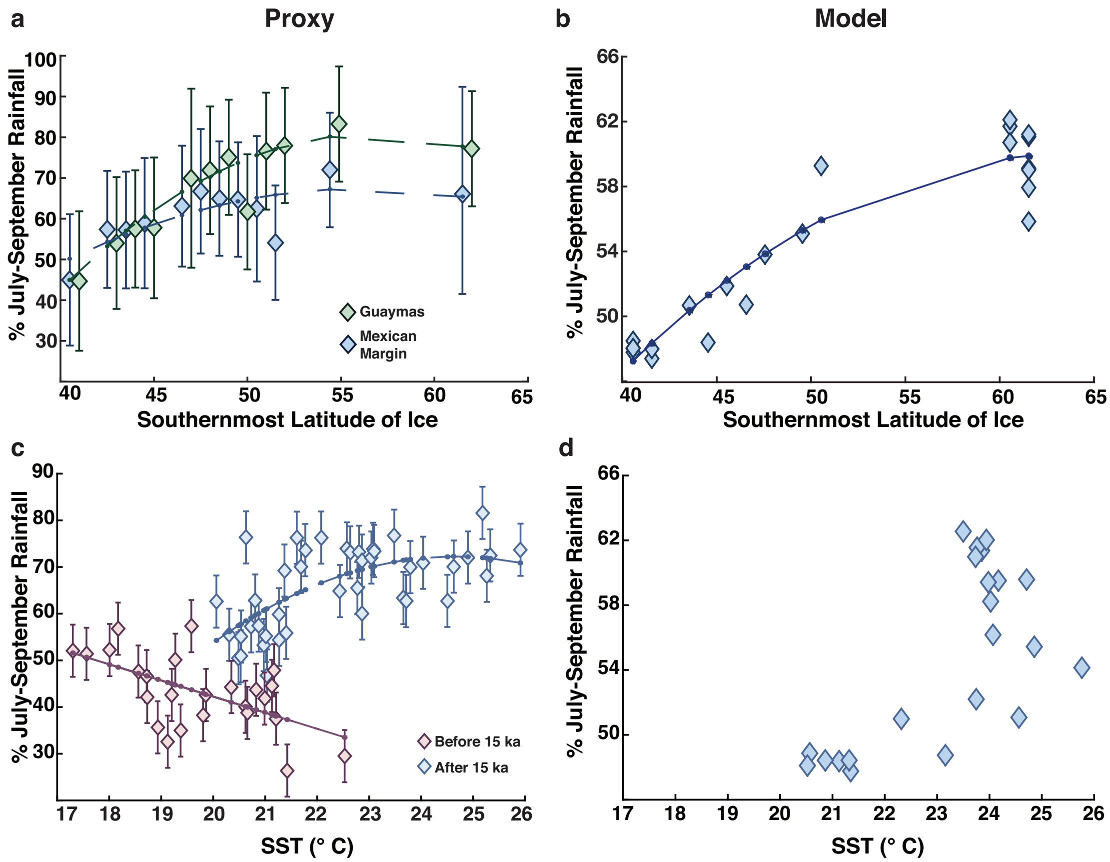

Figure 4: Atmospheric and oceanic drivers of glacial NAM changes. a) % July-September rainfall vs. the southernmost latitude of ice cover. Error bars represent 95% confidence intervals for % July-September values. b) Modeled NAM-region % JAS sensitivity to ice extent across HadCM3 simulations. c) Guaymas Basin % July-September rainfall vs. SSTs, in contrast to d) modeled relationship between SST and % July-September rainfall averaged between 102-112°W and 20-35°N.